drones

MDPI

Article

Numerical Analysis and Wind Tunnel Validation of Droplet Distribution in the Wake of an Unmanned Aerial Spraying System in Forward Flight

Manuel Carreño Ruiz *, Nicoletta Bloise, Giorgio Guglieri and Domenic D'Ambrosio

Department of Mechanical and Aerospace Engineering, Politecnico di Torino, Corso Duca degli Abruzzi, 24, 10129 Torino, Italy

* Correspondence: manuel.carreno@polito.it

Abstract: Recent developments in agriculture mechanization have generated significant challenges towards sustainable approaches to reduce the environmental footprint and improve food quality. This paper highlights the benefits of using unmanned aerial systems (UASs) for precision spraying applications of pesticides, reducing the environmental risk and waste caused by spray drift. Several unmanned aerial spraying system (UASS) operation parameters and spray system designs are examined to define adequate configurations for specific treatments. A hexarotor DJI Matrice 600 equipped with T-Motor "15 × 5" carbon fiber blades is tested numerically using computational fluid dynamics (CFD) and experimentally in a wind tunnel. These tests assess the aerodynamic interaction between the wake of an advancing multicopter and the fine droplets generated by atomizers traditionally used in agricultural applications. The aim of this research is twofold. First, we analyze the effects of parameters such as flight speed (0, 2, and 3 m·s^{-1}), nozzle type (hollowcone and fan), and injection pressure (2–3 bar) on spray distribution. In the second phase, we use data from the experimental campaign to validate numerical tools for the simulation of rotor–droplet interactions necessary to predict spray's ground footprint and to plan a precise guidance algorithm to achieve on-target deposition and reduce the well-known droplet drift problem.

Keywords: unmanned aerial systems; experimental testing; CFD simulation; multiphase flow; precision agriculture

check for updates

Citation: Carreño Ruiz, M.; Bloise, N.; Guglieri, G.; D'Ambrosio, D. Numerical Analysis and Wind Tunnel Validation of Droplet Distribution in the Wake of an Unmanned Aerial Spraying System in Forward Flight. *Drones* **2022**, *6*, 329. https://doi.org/10.3390/drones6110329

Academic Editors: Görres Grenzdörffer and Jian Chen

Received: 15 September 2022
Accepted: 24 October 2022
Published: 29 October 2022

Publisher's Note: MDPI stays neutral with regard to jurisdictional claims in published maps and institutional affiliations.

Copyright: © 2022 by the authors. Licensee MDPI, Basel, Switzerland. This article is an open access article distributed under the terms and conditions of the Creative Commons Attribution (CC BY) license (https://creativecommons.org/licenses/by/4.0/).

1. Introduction

Now more than ever, the agricultural sector has a growing responsibility connected with global demographic growth and the vast increase in food production requirements. In particular, in recent years, the concept of precision agriculture (PA) has become increasingly important thanks to the fourth agricultural revolution and the progress of technology. Regarding environmental protection and climate change, PA focuses on reduced natural resources and the causes of resistance to chemical products. In parallel, the technological evolution of farm machinery and communication systems allows increasing the automation level in complex environments within sustainable agriculture, as discussed in [1,2].

Nowadays, for some automatic operations, unmanned aerial systems (UASs) may be advantageously combined with conventional machines, helicopters, and/or human operators. In [3], the authors provide a detailed review of UAS applications for precision agriculture. Several aspects and technologies for various systems and payloads are studied in depth, concentrating on aerial crop monitoring and spraying operations. Therefore, the focus of this paper is to study the spray system integrated on a UAS and its relative spray field under the rotor wake to evaluate the best operational parameters to carry out precision crop spraying in vineyards. A preliminary design of this concept of rotary-wing unmanned aerial spraying systems (UASS) is presented by the authors in [4].

For three decades, aerial spray operations with UASSs have been proliferating in some Asian countries, starting from Japan and expanding into South Korea and China [5] and then worldwide. Regarding high accessibility and popularity, early research was done in Asia on flat rice and corn canopies, where uniform distribution and good penetration are more critical than precision coverage. Nevertheless, since the advent of agricultural spraying, a crucial challenge has always been the drift problem (i.e., the sprayed pesticides that miss the target) that is becoming very important to evaluate the risk assessment of pesticide processes. Several researchers [6–9], among others, have explored most factors that influence this phenomenon, such as flight altitude and speed, nozzle type, injection pressure, and wind speed. Reference [10] shows an extension to a static configuration. The authors present the results of a UASS adapting control law under changing weather conditions to guarantee precise pesticide deposition. Reference [11] focuses attention on the effect of wind on spray distribution and proposes an adaptive guidance algorithm in a windy environment. The real difficulties related to a more specific request regarding droplet position arise with 3D crops, usually placed in rows, such as orchard trees. For this canopy, the risk of off-target losses increases, and it is even more interesting to investigate the influence of the flight and spray parameters to obtain the required pesticide distribution and penetration of the canopy for different crops, as shown in [12–15]. Optimizing spray management in vineyards is of interest as they can be characterized by sloped and irregular terrain and arranged in long narrow rows, as analyzed in [16]. This creates many challenges, resulting in more complex precision spraying operations and the flight mode being crucial to maximizing the product deposition on the crop and minimizing the drift towards the inter-row region. Additionally, in [17], the authors investigate vineyard spray deposition and coverage due to different operational parameters. However, the limited payload availability makes the UAS advantageous only in critical areas that are difficult to reach by other machines. Human operators are forced to go and are exposed to hazardous products.

The interaction between spray and rotors has been experimentally tested both in the open field [18] and in wind tunnel facilities [19,20], where the authors investigate drift with varying wind speed, spray volume, and nozzle characteristics. Drift is also addressed in [21], where the authors survey solutions to reduce the inevitable drift by optimizing the rotor, nozzle setup, spray system, and flight parameters. In parallel with experiments, numerical simulations have been performed to investigate the downwash flow field of multi-rotors. A lattice Boltzmann approach is used in [22] to study the wake behind a plant protection hexacopter. Other computational approaches also include the study of droplet trajectories modeled using a dispersed phase model (DPM), as shown in [23–25]. The authors of [26] show a similar approach by injecting Lagrangian particles into the wake of a hexacopter. We emphasize how the Lagrangian particle model requires injection inputs, such as droplet diameter, momentum, and spray angle, which are a priori unknown and difficult to predict accurately. The authors also present a complete UASS design and mission guidelines for a spraying operation in [27].

This paper, which follows the preliminary results shown by the authors in [26], presents the experimental testing of a hexarotor in a wind tunnel facility and has a twofold objective: (a) obtaining a preliminary understanding of the influence of placing the nozzles under the rotors and (b) validating a numerical model able to predict droplet distributions. The first objective is relevant to quantifying the spray cone angle that characterizes hollow-cone nozzles, which is instrumental to the definition of the flight altitude that minimizes deposition of PPP in the inter-row region in vineyards. The second objective aims to define a general framework to test virtually any UAS flight configuration. Such a simulation environment will allow complete simulations specifying flight conditions and spray system parameters, thus allowing us to evaluate the spray distribution before moving to the vineyard. Such an outcome reduces the number of field tests, which are expensive in terms of time and cost.

The results of this experimental campaign are used to analyze the effect of different variables involved in the spraying process, such as nozzle type, injection pressure, advance

velocity, or rotor velocity. LED backlighting is used to visualize the flow and capture some spray characteristics that help us validate a numerical model. For this purpose, a CFD model simulating the flow inside the wind tunnel, including the hexarotor, is presented. Droplets are modeled using spherical Lagrangian particles. The difficulties in determining the inputs shown in [26] are addressed. In this work, the model inputs are estimated by fusing data provided by nozzle manufacturers, experimental observations, and simulations of the hollowcone nozzle using a volume-of-fluid (VOF) approach as shown in [28,29].

This paper is organized as follows. Section 2 includes a description of the material and methods used during the experimental campaign and a thorough explanation of the numerical methods employed in the setup of the CFD model. Section 3 presents the methodology employed during this research and the processed results. Section 4 shows both the data fusion from VOF simulations of the hollowcone nozzle and the manufacturer's data plus the final CFD simulation of the UAS inside the wind tunnel, comparing the predicted aerial spray field with the experimental one. Section 5 presents a discussion of the results of the experimental and numerical campaigns, focusing on the strengths of the numerical model through analyzing the CFD simulations to extract preliminary recommendations for UASS best practices regarding nozzle positioning and operating conditions. Finally, our conclusions are discussed in Section 6.

2. Materials and Methods

In this section, we describe in detail the materials and methods used to reach the objectives of this work. During the activity, we carried out a wind tunnel experimental campaign in a controlled environment with a commercial drone equipped with a dedicated spray system and, in parallel, numerical simulations of the same setup and conditions. Comparing experimental and numerical results allowed us to validate the CFD model of spray distribution in a virtual environment for a specific hollowcone nozzle.

2.1. Wind Tunnel Facility

The SEASTAR-WT (Sustainable Energy Applied Sciences, Technology, and Advanced Research Wind Tunnel) facility at the Environment Park in Turin, Italy, is an atmospheric and subsonic open-circuit wind tunnel that draws air from outside the building through a convergent intake and expels it from a divergent outlet driven by ten fans with an installed capacity of about 100 kW, placed after the divergent. The test section size is 6.4 m in width and 2.4 m in height. A detailed description of the wind tunnel facility is shown in [30]. The relatively large dimensions of the test chamber and the possibility to tune up to a wind velocity of 8 $m \cdot s^{-1}$ allowed us to perform our testing campaign. In particular, a structure was included in the experimental setup to hang the drone from the top of the test section to avoid disturbances in the free stream in the neighborhood of the drone, as shown in Figure 1.

Figure 1. UASS and camera setup in the SEASTAR wind tunnel.

2.2. Specifications of UASS

A customized standalone spray system is designed for a DJI Matrice 600 hexacopter (DJI, Shenzhen, China) and integrated for the experimental test in the wind tunnel, as in Figure 2.

Figure 2. DJI Matrice 600 with customized spray system.

For this purpose, the original blades were replaced with the smaller T-Motor "15 × 5" blades to reduce thrust and to avoid compromising the structure supporting the drone. To properly validate the numerical model, precise blade geometry was needed. An optical precision measuring machine (OPMM) was used to perform a 3D scan of the blade geometry, as shown in Figure 3.

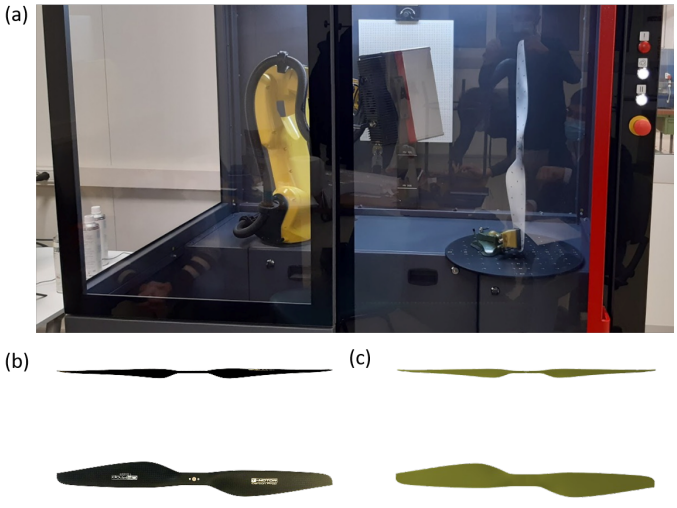

Figure 3. (**a**) Optical precision measuring machine, (**b**) photo of T-Motor "15 × 5" blades, (**c**) point cloud data.

2.2.1. DJI Matrice 600

The DJI Matrice 600 was chosen for the experimental testing campaign. It has a recommended maximum take-off weight (MTOW) of 15.5 kg, and its main characteristics are reported in Figure 4 and Table 1. As shown in Figure 4, the drone is fixed to the supporting frame with its nose, represented with red motors (M1–M2), and rotated clockwise by 30° with respect to the wind direction. The UAS is in a horizontal position relative to the ground. This work does not consider the effect of the tilt angle, a parameter dependent on the weight of the UASS and which decreases during spraying. Accurate measurement of

this angle is challenging, and instead of fixing the tilt angle at an arbitrary angle, as done in other studies, we decided to set the tilt angle to zero.

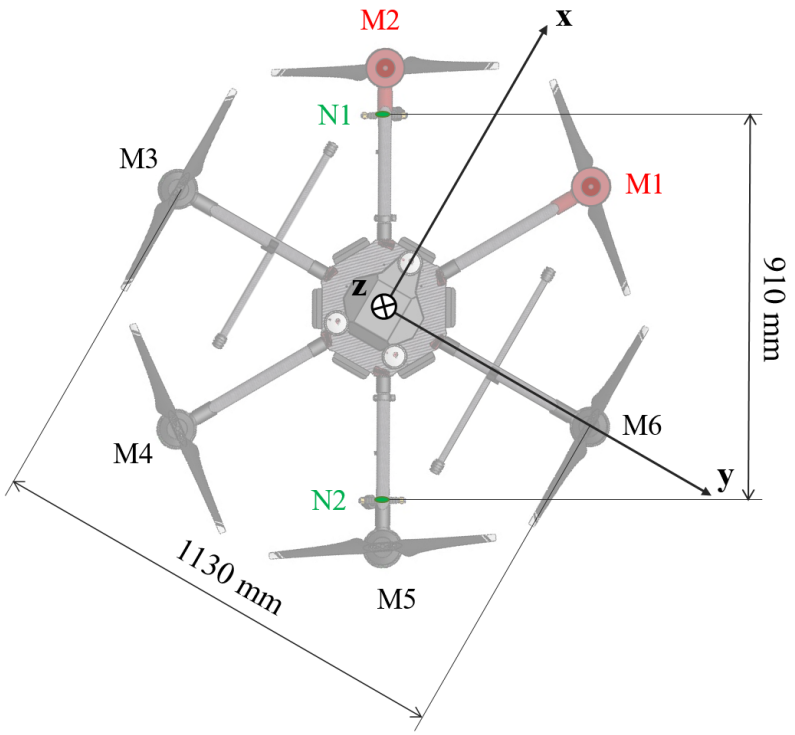

Figure 4. Top view of DJI Matrice 600 (body-fixed axes) with nozzles aligned with wind direction.

At idle, the rotor speed is 1590 RPM, whereas at full throttle, the rotors turn at 5100 RPM. Furthermore, the rotor plane is inclined by 7° with respect to the ground, and this angle influences the spray distribution.

Table 1. Main parameters of DJI Matrice 600.

Parameter Description	Value
Wheelbase	1133 mm
Rotor diameter	381 mm
Rotor pitch	127 mm
Number of rotors	6
Brushless motor	DJI 6010

2.2.2. Spray System Design

A dedicated spray system was manufactured according to the circuit presented in Figure 5 and includes a remote-control system to switch the pump on and off. The system contains a battery, membrane pump, pressure regulator, pressure gauge, and two nozzles for a total weight of approximately 2.5 kg. In particular, the external battery powers the membrane pump to generate a maximum flow rate of 6 L/min, which can be switched on/off by a radio remote control. A manual pressure regulator is downstream of the pump. Finally, a vacuum pressure gauge measures the pressure level in real-time to guarantee the correct liquid flow rate of the nozzles. Two nozzle holders (N1 and N2) are installed under the M2 and M5 rotors, as evidenced in Figure 4, perpendicular to the rotor arms. Hollowcone (HCI8002, manufactured by ARAG Group) and anti-drift fan nozzles (AFC11002, manufactured by ARAG Group (Rubiera, Italy) are tested to analyze relative spray characterization. In this figure, the coordinate system (x, y, z) represents the body axes, complying with the reference frame that the DJI company specifies for the flight

controller. The UASS is rotated clockwise by 30° because in this application the nozzles must be precisely above the vine rows and therefore aligned with the wind direction.

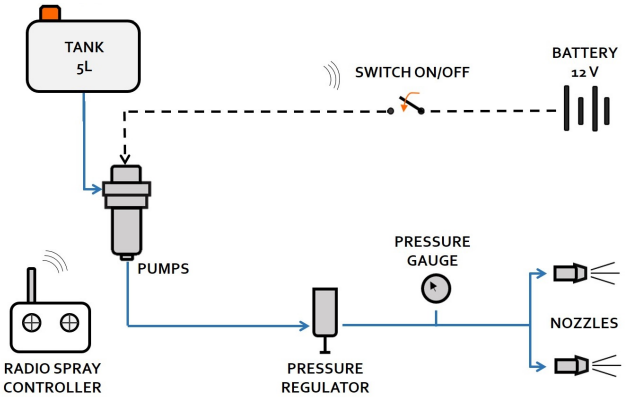

Figure 5. Hydraulic circuit of spraying system.

2.3. Experimental Campaign

Table 2 shows the test matrix for the experimental campaign in the wind tunnel. We can distinguish 24 different test conditions. The images showing droplet visualization corresponding to these tests can be found in the following section.

Table 2. Experimental test matrix.

TEST I.D.		Wind Speed ($m \cdot s^{-1}$)			Nozzle Type		Motor Speed			Pressure	
Name	**#**	**0**	**2**	**3**	**HCI8002**	**AFC11002**	**0**	**Idle**	**Max**	**2 bar**	**3 bar**
HCI_v0_0_2	1	X			X		X			X	
HCI_v0_I_2	2	X			X			X		X	
HCI_v0_T_2	3	X			X				X	X	
HCI_v2_0_2	4		X		X		X			X	
HCI_v2_I_2	5		X		X			X		X	
HCI_v2_T_2	6		X		X				X	X	
HCI_v3_0_2	7			X	X		X			X	
HCI_v3_I_2	8			X	X			X		X	
HCI_v3_T_2	9			X	X				X	X	
AFC_v0_0_2	10	X				X	X			X	
AFC_v0_I_2	11	X				X		X		X	
AFC_v0_T_2	12	X				X			X	X	
AFC_v2_0_2	13		X			X	X			X	
AFC_v2_I_2	14		X			X		X		X	
AFC_v2_T_2	15		X			X			X	X	
AFC_v3_0_2	16			X		X	X			X	
AFC_v3_I_2	17			X		X		X		X	
AFC_v3_T_2	18			X		X			X	X	
HCI_v0_0_3	19	X			X		X				X
HCI_v0_I_3	20	X			X			X			X
HCI_v0_T_3	21	X			X				X		X
AFC_v0_0_3	22	X				X	X				X
AFC_v0_I_3	23	X				X		X			X
AFC_v0_T_3	24	X				X			X		X

2.3.1. Methodology

Flow visualization was performed employing LED illumination with a high output of luminous flux of 4500 lm. The light source was positioned to shoot backlighting photos obtaining a qualitative analysis of droplet distribution, as illustrated in Figure 6. Lateral and frontal photos are taken from a Nikon D750 with 6016 × 4016 pixels resolution.

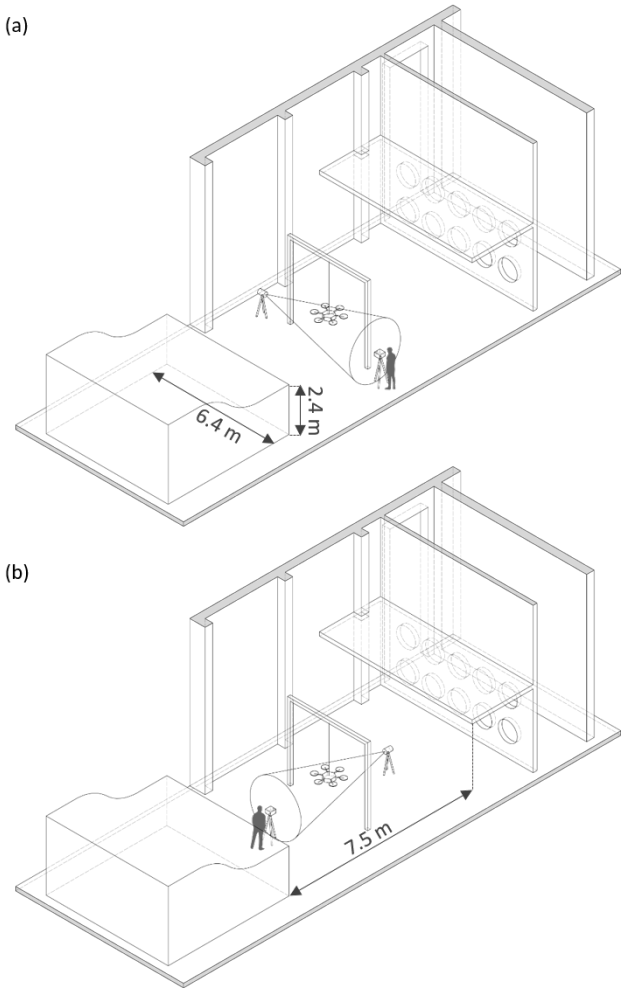

Figure 6. Spray visualization with LEDs in the wind tunnel: (**a**) lateral view and (**b**) frontal view.

2.3.2. Data Analysis

The automated process with which the images are analyzed allows us to extract relevant data and is divided into three phases:

- The RGB photos are converted into grayscale images and are then filtered to obtain binary images, as shown in Figures 7(1) and 8(1), by applying an intensity threshold.
- The binary image is block-processed, as shown in Figures 7(2) and 8(2). They are divided into small squares, and the number of white pixels corresponding to droplets is counted. If the percentage of these white pixels is greater than a fixed threshold, the pixel concerned is considered part of the spray cone. Otherwise, it is discarded and colored completely black. This procedure eliminates stray droplets and determines all the points needed for trajectory fitting. Then, the images are divided into horizontal rows, and the rightmost and leftmost white pixels of each row are memorized as the limits of the spray cone. The process is repeated by columns, and the pixels that verify both conditions are considered to be in the contour.
- A polynomial fitting of the contour points is performed to approximate the spray shape, as shown in Figures 7(3) and 8(3).

The lack of spatial resolution in the normal direction to the plane of the images and the aim of having a large field of view prevents us from performing more quantitative measurements that require spatial and temporal tracking of individual droplets. Therefore, the validation of the numerical approach will only be based on the contrast spray contours revealed in the lateral views.

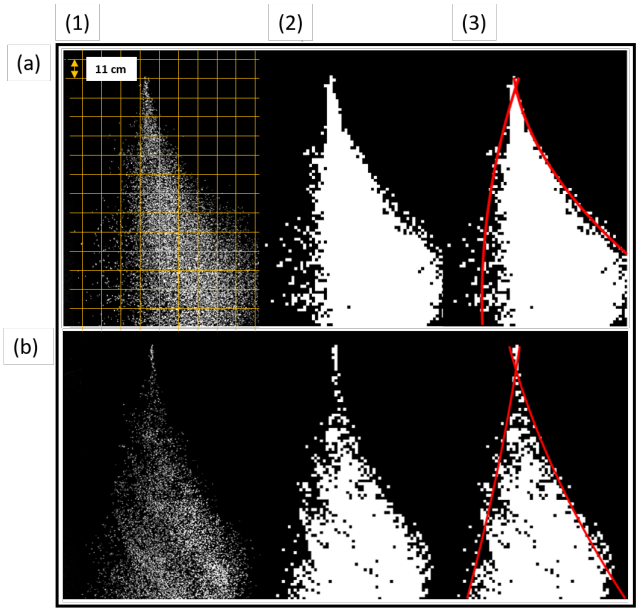

Figure 7. Spray with fan nozzle at $V = 2$ m·s^{-1} at (**a**) $RPM = 1590$ and (**b**) $RPM = 5100$.

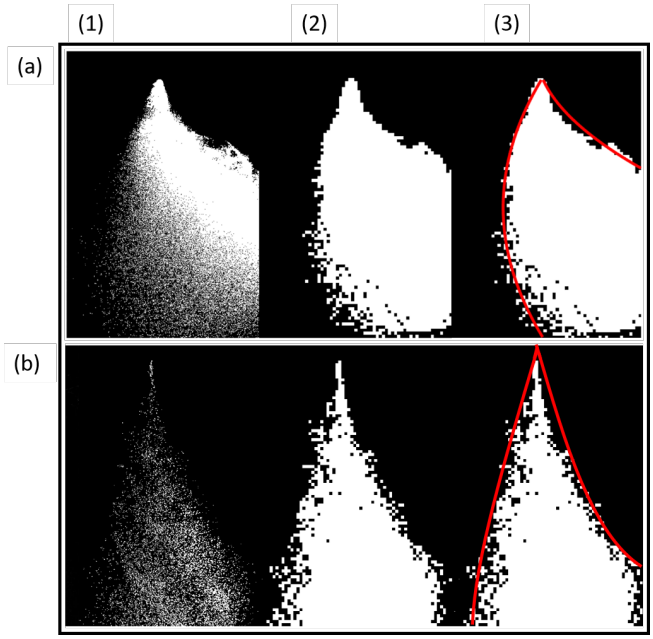

Figure 8. Spraywith hollowcone nozzle at $V = 2$ m·s^{-1} at (**a**) $RPM = 1590$ and (**b**) $RPM = 5100$.

2.4. Numerical Methods

The numerical model used to simulate the flow inside the wind tunnel are the unsteady Reynolds-averaged Navier–Stokes (URANS) equations embedded in the commercial CFD software STARCCM+ [31]. An accurate CAD model replicating the experimental approach is the base for the numerical model. The rotational motion of the rotors is modeled with a dynamic mesh approach in which a portion of the grid embedding the rotor slides inside an outer static grid using an arbitrary nesh interface (AMI) protocol. This approach has been validated in [32–34]. The generated mesh consists of 10 million cells. The region occupied by the leading rotor and its wake contains around four million cells to increase the resolution and obtain an accurate description of the jet that subsequently encounters the injected particles. The time step is defined to allow a maximum rotation of 3°. The resulting value has an order of magnitude of 10^{-4} s. The flow in the wind tunnel is allowed to evolve for 60 s with the rotor off with a larger time step. Then, the rotors are allowed to rotate for

a total of 4 s: first 2 s before the particles are injected and then an extra 2 s with droplet injection. The adopted time-integration scheme is implicit and second-order accurate. The spatial accuracy is also second order. As a turbulence model, we use the one-equation Spallart–Allmaras model [35]. The generated grid has y^+ values lower than 1, in agreement with the turbulence model guidelines. The flow in the wind tunnel is driven by ten fans, as shown in Figures 1 and 6. These are modeled with a fan-type interface that assumes a finite pressure jump across a zero-thickness disk. The pressure jump is computed based on the fan performance curve supplied by manufacturers shown in Figure 9. The performance curve can be adjusted for different operating rotational velocities of the fans, which allows adjustment of the velocity magnitude in the test section. The usual linear scaling for flow rate and quadratic scaling for pressure jumps predicted by actuator disk theory is used, as shown in Equations (1) and (2).

$$\Delta P_2 = \Delta P_1 \frac{\Omega_2^2}{\Omega_1^2} \tag{1}$$

$$V_2 = V_1 \frac{\Omega_2}{\Omega_1} \tag{2}$$

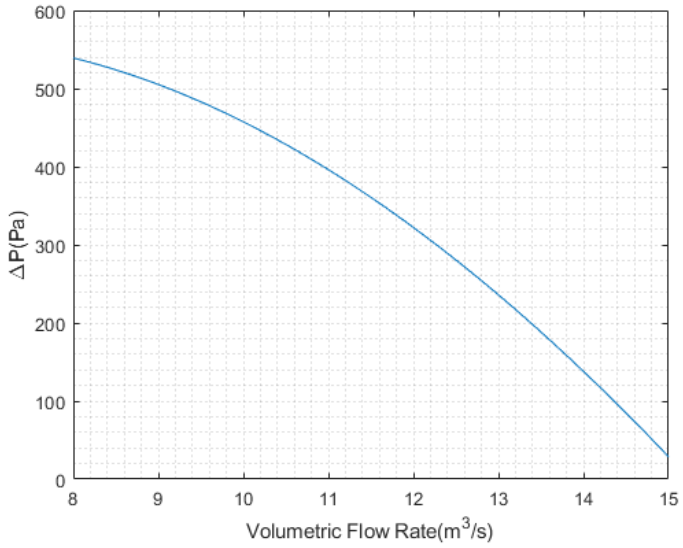

Figure 9. Fan performance curve at 1700 RPM.

Figure 10 shows the velocity field inside the wind tunnel driven by the fans, including the UAS operating at 5100 rpm. The wind velocity at the center of the test section inside the wind tunnel with the rotors off was measured to be 2.0 m·s^{-1}. This value compares well with the velocity of 1.96 m·s^{-1} revealed by the CFD simulation at the same position.

The spray droplets injected in our simulations are modeled with Lagrangian spherical particles. The linear momentum conservation law, shown in Equation (3), is solved:

$$m_p \frac{\mathbf{v}_p}{dt} = \mathbf{F}_g + \mathbf{F}_{vm} + \mathbf{F}_d + \mathbf{F}_p + \mathbf{F}_{sl} \tag{3}$$

where the forces acting on the particle are, from left to right, gravity, virtual mass, drag, pressure gradient, and shear lift. The drag coefficient proposed in [36] is used to compute the drag force. For calculation of the shear lift, the expression provided in [37] is employed.

The initial conditions for integrating the conservation laws are computed using multiphase high-resolution interphase capturing VOF in a separate CFD simulation of the employed nozzle. This methodology has been followed by [28,29], among others, to compute spray characteristics. This approach solves an extra scalar transport equation for the volume fraction, as shown in Equation (4).

$$\frac{\partial \alpha}{\partial t} + \nabla \cdot (\alpha \mathbf{u}) = 0 \tag{4}$$

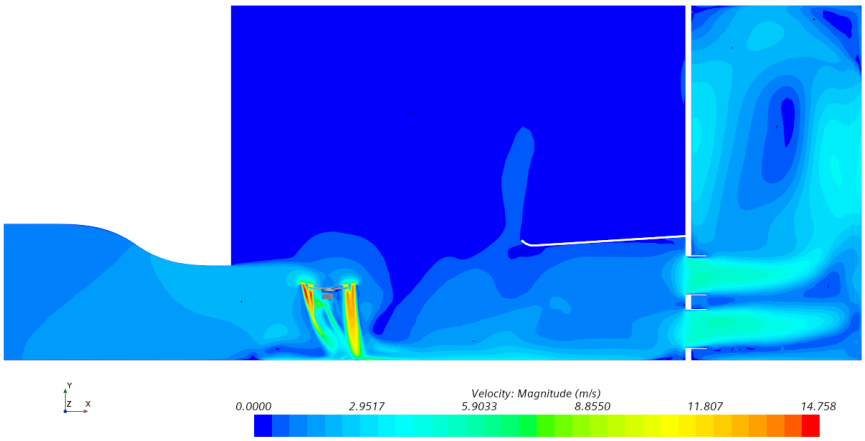

Figure 10. Instantaneous velocity magnitude field inside the wind tunnel operating at 2 m·s^{-1} and with rotors operating at 5100 RPM.

The volume fraction is an indicator function that defines the phase. A value of 1 corresponds with "phase 1" (water), and a value of 0 corresponds with "phase 2" (air). The interphase can be defined by a volume fraction value of 0.5. The cells in the interphase region must be refined to capture a sharp interphase. For this purpose, adaptive mesh refinement (AMR) is implemented to capture the water–air interphase without the necessity of refining the whole computational domain. The average number of cells in the fully developed flow is around 5 million. The continuum surface force (CSF), first described by Brackbill [38], is included to model the surface tension, which is known to be necessary to reproduce atomization [39] adequately. The Courant–Friedrich–Levy (CFL) number should be kept below 1, even for implicit time integration schemes, to avoid interphase blurring. In addition, to avoid this restrictive condition on the time step, a multi-stepping approach for the volume fraction transport equation is used, allowing the global CFL condition to be relaxed and reducing the computational cost of the simulations. Even with this improvement, the time-step must remain around 10^{-6} s, which generates considerable computational cost.

We perform the simulations using 64 cores of 2 Intel Xeon Scalable Processors Gold 6130 2.10 GHz. The computational cost of the simulation of the hexacopter spraying operation inside the wind tunnel is around 6000 CPU hours, and the multiphase simulations of the hollowcone nozzle last approximately 12,000 CPU hours.

3. Experimental Results

Figures 11 and 12 show the most significant lateral photos taken during testing. Following the test matrix, the cases of hollowcone and fan nozzle are presented by varying RPM and wind velocities.

Likewise, Figures 13 and 14 represent some results of frontal photos to evaluate the reduction of spray angle with the increase of rotor RPM or pressure.

The first outcome that can be extracted from the presented results is the influence of the rotors' wake on droplet distribution. As the rotor speed increases, the spray distribution is more controlled and vertical, which is a clear advantage for the vineyard scenario. In addition, wind velocity and rotation rate influence with the hollowcone nozzle is much more substantial than with the fan nozzle. The droplets produced by the hollowcone nozzle are finer; consequently, they are more subject to drift with the flow than those produced by a fan nozzle.

These results validate the CFD model that predicts the particle distribution. Once that is done, it could be valuable to explore other conditions to avoid the time and economic costs that an experimental campaign requires.

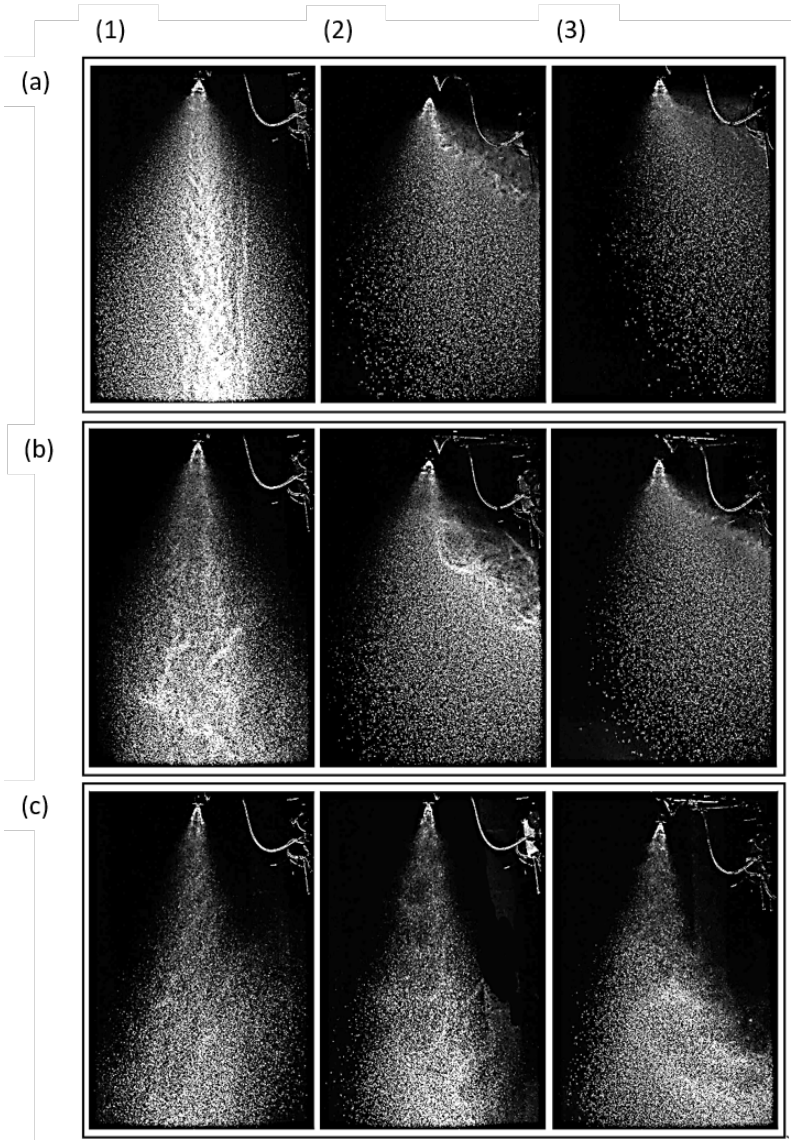

Figure 11. Lateralview of spray with hollowcone nozzle for (**a**) no rotor, (**b**) idle, and (**c**) throttle condition in (**1**) hovering, (**2**) at wind speed = 2 m·s^{-1}, and (**3**) at wind speed = 3 m·s^{-1}.

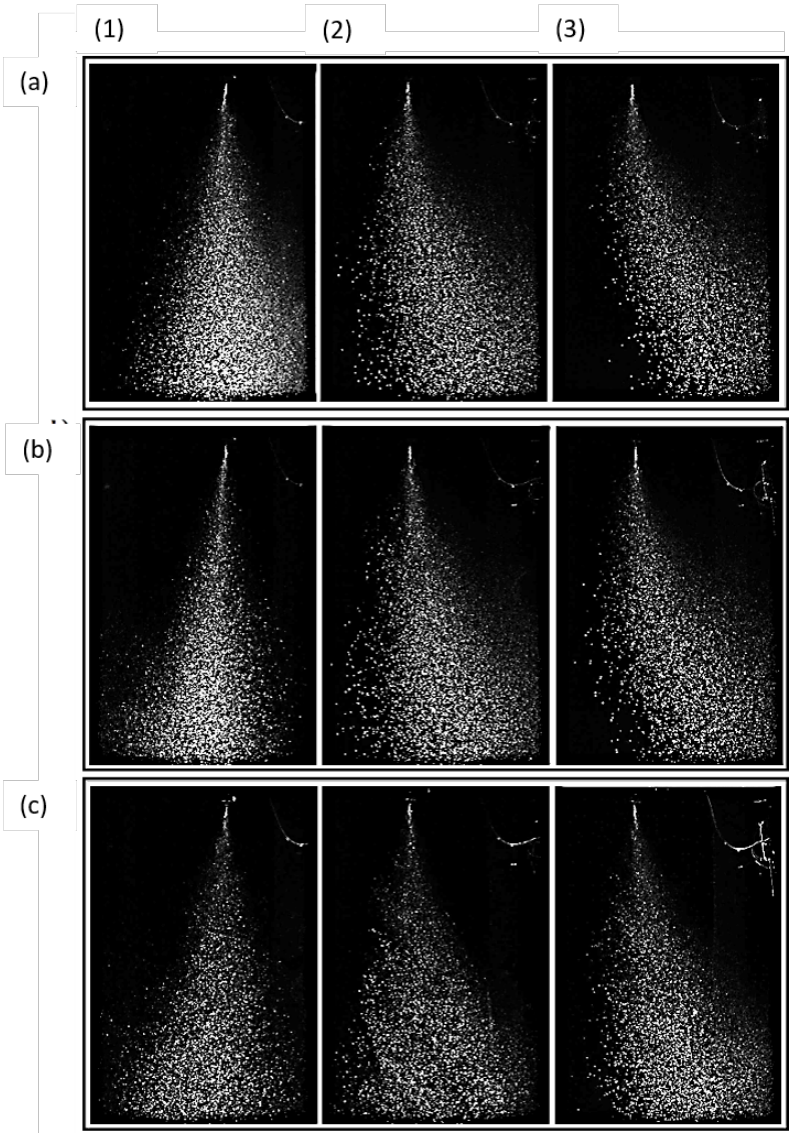

Figure 12. Lateral view of spray with fan nozzle for (**a**) no rotor, (**b**) idle, and (**c**) throttle condition in (**1**) hovering, (**2**) at wind speed = 2 m·s^{-1}, and (**3**) at wind speed = 3 m·s^{-1}.

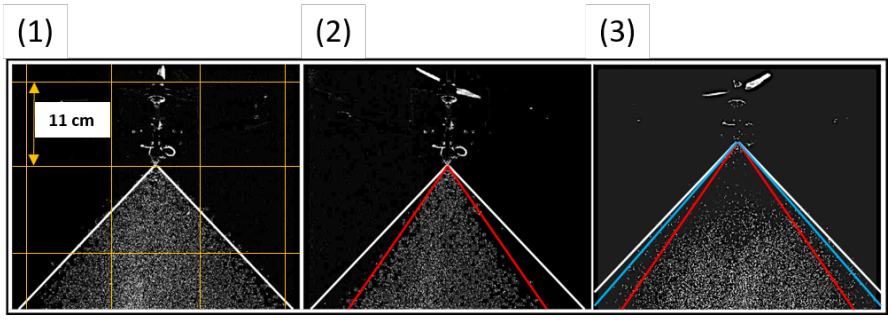

Figure 13. Frontal view of spray with fan nozzle for (**1**) no rotor at 2 bar, (**2**) throttle at 2 bar, and (**3**) throttle at 3 bar.

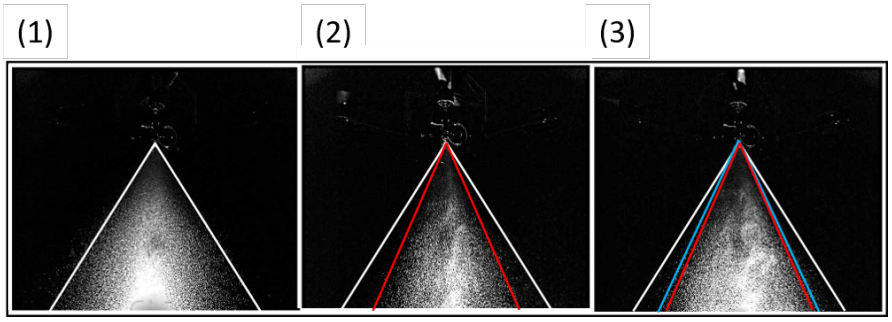

Figure 14. Frontal view of spray with hollowcone nozzle for (**1**) no rotor at 2 bar, (**2**) throttle at 2 bar, and (**3**) throttle at 3 bar.

4. CFD Simulation: Hollowcone Nozzle

In this section, the CFD validation is conducted exclusively for the hollowcone nozzle, but the same methodology could be applied to other types of nozzles.

4.1. Pressure-Swirl Atomizers

The hollowcone nozzle used in the experimental campaign is provided by ARAG Group with reference code HCI8002. This nozzle is classified as a pressure-swirl nozzle as a conical sheet of fluid is formed at the nozzle exit due to the centrifugal forces actuating in the rotating fluid inside the swirl chamber. The breakdown of the conical sheet first into ligaments and then into droplets is a very complex physical process that is highly complex and expensive to model numerically [39]. Several authors, such as [28,29], have employed interphase capturing methods to resolve the conical sheet formation and even the ligament and particle breakdown. Four main characteristics define a hollowcone spray: (i) particle diameter distribution, (ii) film velocity,(iii) film thickness, and (iv) cone angle. These parameters are strongly influenced by the injection pressure/mass flow and the nozzle geometry, especially by the exit orifice. Determining the hollowcone spray characteristics is mandatory to model the interaction between the rotors and the spray. A simplified CAD model of the nozzle is shown in Figure 15, and the main characteristics are shown in Table 3.

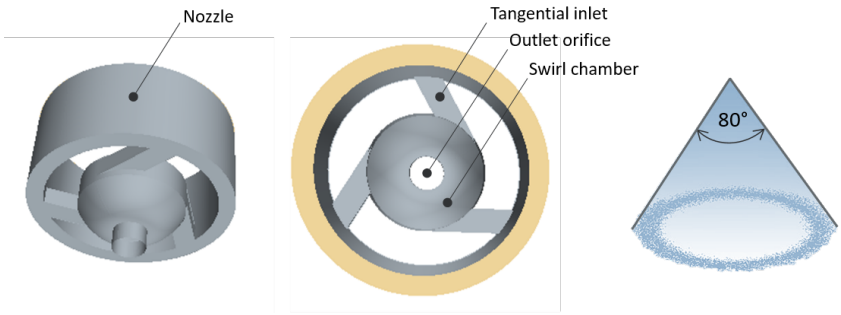

Figure 15. CAD model and hollowcone spray angle of the HCI8002 nozzle.

Table 3. Main characteristics of the HCI8002 nozzle.

ARAG–HCI8002	
Pressure	3 bar
Volume flow rate	0.8 L min^{-1}
Droplet size	fine

This model represents the inner geometry of the nozzle and has been developed to allow an accurate CFD modeling of the multiphase flow. This nozzle comprises three tangential inlets that rotate the flow around the vertical axis in the swirl chamber. The centrifugal forces

push the fluid towards the wall, generating an air core inside the nozzle. When pressure builds up and this rotating liquid film is forced through the orifice, the centrifugal forces expand the liquid film, forming a conical fluid film, as shown in Section 4.1.2.

4.1.1. Droplet Diameter Distribution

The nozzle manufacturers have provided the particle diameter distribution for several injection pressures. Figure 16 shows the particle diameter distribution extrapolated to our working pressure of 2 bar using a 3-point-based Akima algorithm [40] for each droplet diameter. We can appreciate how the particle diameter approximates a log-normal distribution with parameters $\mu = 5.11$ and $\sigma = 0.52$.

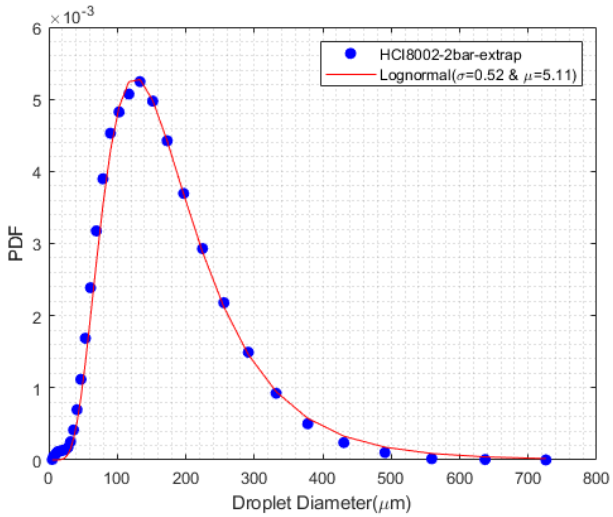

Figure 16. Probability density function for droplet diameter distribution.

4.1.2. Cone Angle

Our visualization technique, described in Section 2.3.1, allows experimental determination of the outer angle of the conical sheet of liquid, which becomes unstable and breaks down initially into ligaments and then into droplets [28]. Frontal images are used to measure the cone angle, as shown in Figure 17. We can appreciate an angle of approximately 79 degrees.

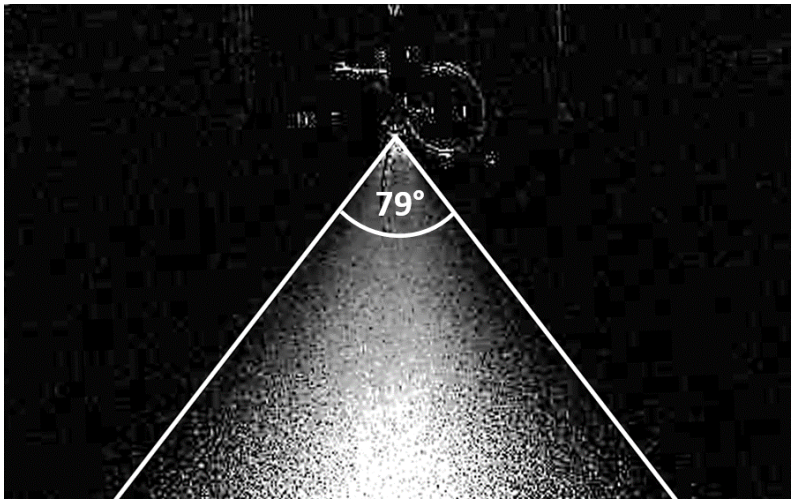

Figure 17. Hollowcone angle for a pressure of 2 bar measured during the experimental campaign.

Figure 18 shows the water–air interphase, which clearly shows a hollowcone shape, and this value agrees well with the cone angle found in the CFD simulation shown in

Figure 19, where a half-cone angle of 40 degrees is measured. The atomization process is reproduced and shows the breakdown of the conical fluid sheet first into ligaments, and then these ligaments break down into droplets. This image is a detail of the near nozzle region. A much larger domain showing complete atomization is shown in Section 4.2.

Figure 18. Water–air interphase in VOF CFD simulation showing the conical sheet of fluid produced by the pressure swirl nozzle at a pressure of 2 bar.

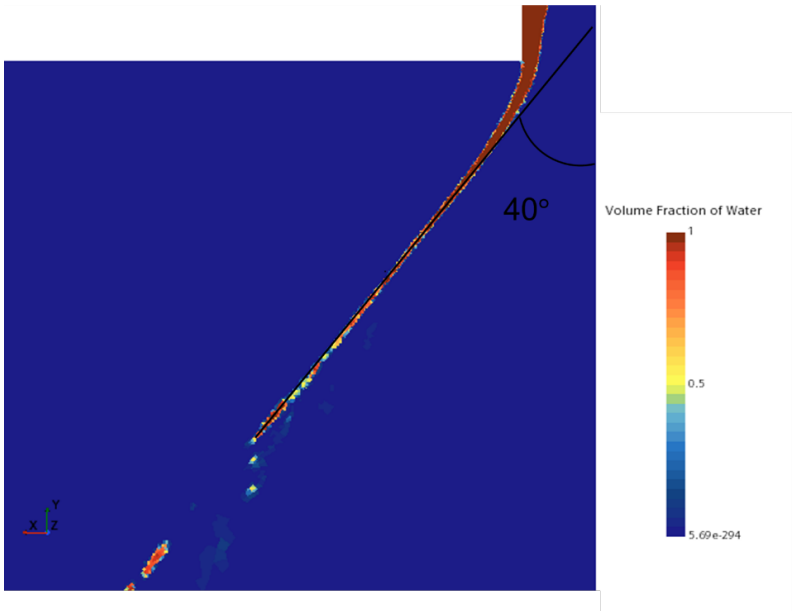

Figure 19. Water volume fraction in VOF CFD simulation showing the conical sheet of fluid produced by the pressure swirl nozzle at a pressure of 2 bar.

4.1.3. Film Velocity and Tangential Velocity

The film velocity is the non-tangential velocity component of the liquid contained in the conical sheet. Considering a cylindrical coordinate system (r, θ, z) centered on the exit orifice and with the z-axis coincident with the vertical axis, the film velocity (U_f) would be the result of combining the radial (U_r) and axial (U_z) components of velocity, as shown in Equation (5).

$$U_f = \sqrt{U_r^2 + U_z^2} \tag{5}$$

The film velocity of the conical sheet calculated in the CFD simulations presents a value of around 14.5 m·s^{-1} before instabilities trigger the breakdown into ligaments and droplets. Even though the simulation time and generated droplets are possibly insufficient to consider statistical convergence, Figure 20 shows that, just after breakdown, droplets present an almost constant initial velocity equal to the film velocity, as most of the droplets present a very close value of between 14 and 15 m·s^{-1}. Therefore, we model Lagrangian particles with a constant injection velocity of 14.5 m·s^{-1}.

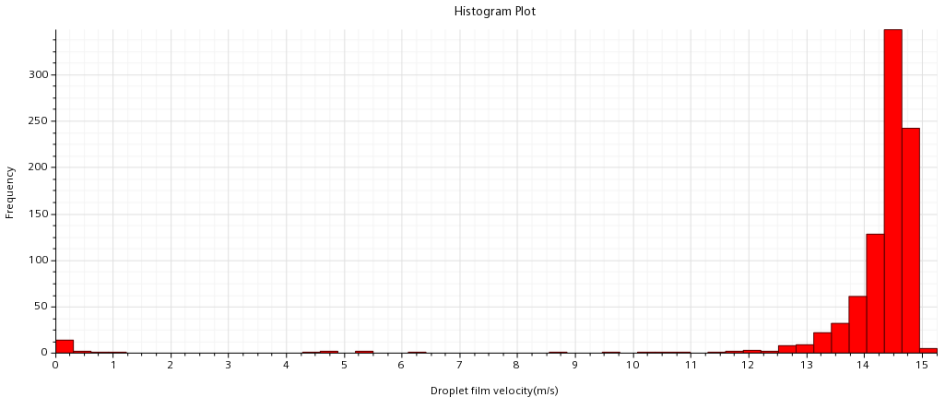

Figure 20. Film velocity of the liquid droplets after the breakdown of the conical sheet of fluid produced by the pressure swirl nozzle at a pressure of 2 bar.

On the other hand, the tangential velocity (U_θ) is not constant as the fluid film evolves and decreases as the radial coordinate of the cone increases, as shown in Figure 21. We can appreciate how the generated droplets have a tangential velocity close to zero. Therefore, we simulate Lagrangian particles without an initial tangential velocity.

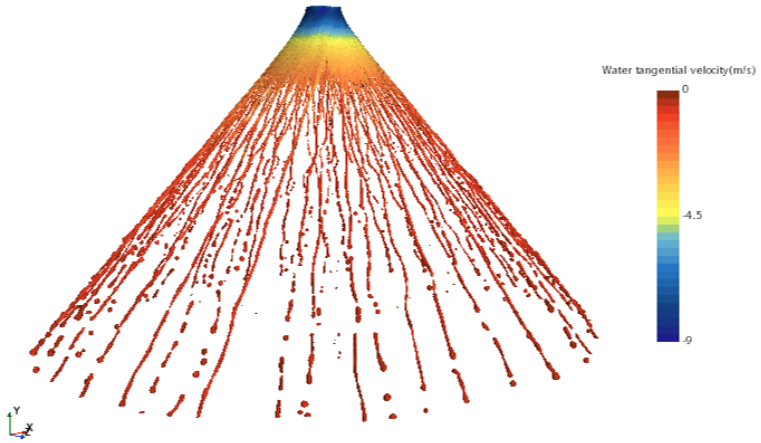

Figure 21. Tangential velocity of the liquid phase forming a conical sheet of fluid produced by the pressure swirl nozzle at a pressure of 2 bar.

4.2. Wind Effects on the Hollowcone Spray

Simulations using the 80-degree cone angle for the injection of Lagrangian particles (not shown in this paper) reveal much wider droplet dispersion compared to the experimental measurements. This finding suggests that the conical sheet is deformed before droplets detach from the ligaments due to the strong rotor induction. Hence, the injection angle of the Lagrangian particles should be modified. To capture the rotor downwash's first-order effects on droplet formation, a multiphase simulation is performed with a constant vertical wind. From simulation of the hexarotor at maximum throttle, the induced axial velocity at the

injection point is found to be 12 m·s^{-1}. This value is used as the vertical velocity in the VOF simulations. Figure 22 shows significant closure of the cone angle from 80° to 56°.

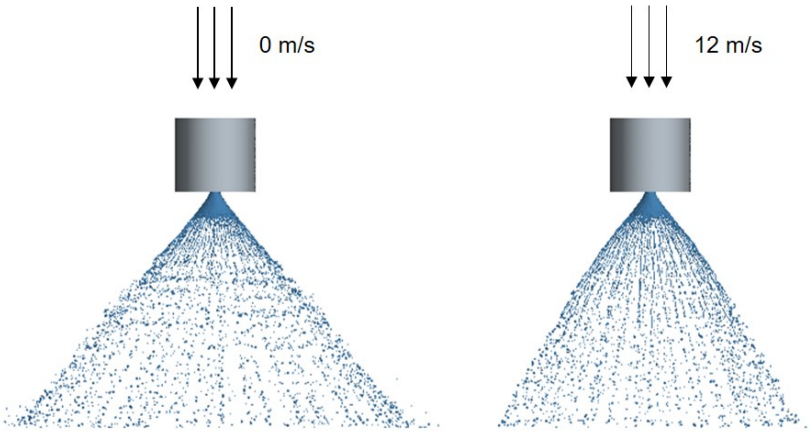

Figure 22. Water–air interphase in VOF CFD simulation showing the conical sheet of fluid produced by the pressure swirl nozzle at a pressure of 2 bar with no axial velocity (**left**) and with an axial velocity of 12 m·s^{-1} (**right**).

Therefore, an angle of 56 degrees is used to model the hollowcone injector of Lagrangian particles.

4.3. Experimental Validation

The previous sections explained how we estimated the initial conditions (momentum, diameter, and cone angle) for the Lagrangian particle injection model. The mass flow rate is set to a value of 0.67 liters per second, as in the VOF simulation. A random number generator following a log-normal distribution with $\mu = 5.11$ and $\sigma = 0.52$ is employed to inject particles with diameters coherent with the statistical distribution extrapolated from manufacturers' data. Particles are injected over 2 s to allow converged statistics and to give time for them to be convected by the flow.

In order to assess the validity of the developed numerical model, we present a comparison between experimental LED visualization images and the distribution of Lagrangian particles. We perform this validation with the wind tunnel operating at 2 m·s^{-1} with the rotors off and operating at maximum throttle. The simulation parameters are summarized in Table 4. Comparison with experimental results is shown in Figure 23.

Table 4. Numerical simulation parameters.

Simulation	Test I.D.	Wind Speed (m·s^{-1})	Nozzle Type	Motor Speed	Pressure
1	HCI_v2_0_2	2	HCI8002	0	2 bar
2	HCI_v2_T_2	2	HCI8002	5100 rpm	2 bar

We can appreciate how the lateral views are congruent, presenting similar cone angles, and the lateral wind-induced drift is evident. The contours of the spray are highlighted in blue for the experimental images and red for the numerical prediction of droplet distributions. The minor deviations of the spray distributions are possibly caused by the fact that in Section 4.2, fully vertical flow was considered, and indeed, a small component of cross-flow would be present that could eventually deform the hollowcone fluid sheet slightly, modifying injection parameters. Another possible source of error is slight misalignment of the injector in the experimental campaign caused by the impulsive activation of the spray system. CFD simulations give additional information, as we can track every particle in the 3D domain. In addition, it is appreciated how the drift is extremely sensitive to particle

diameter. Large particles (red and orange) maintain the conical structure considerably due to their large inertia, making them much less sensitive to the velocity and pressure fields. On the other hand, smaller particles (yellow, green, and blue) are affected by the flow, which convects the droplets upstream and downstream of the hexacopter. However, we appreciate how most of the particles are contained in the wake and how this directs the particles towards the ground, reducing drift. In order to show the beneficial effect of the rotor downwash, Figure 24 shows a comparison of the droplet distributions obtained with and without the rotors operating at full speed.

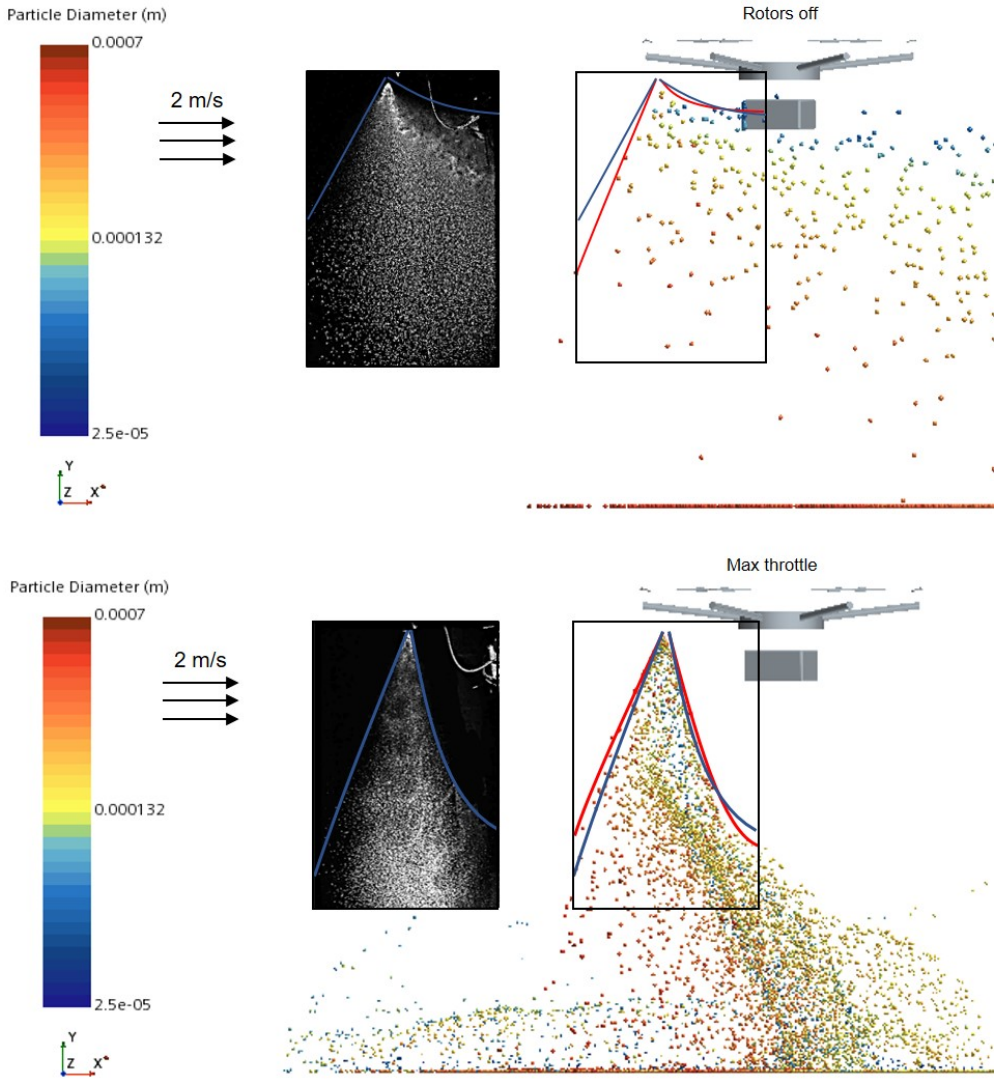

Figure 23. Comparison between the lateral views of droplet LED visualization and CFD simulations with a wind tunnel speed of 2 m·s^{-1} with rotors off (**top**) and rotors at full throttle (**bottom**).

The drift is minimized except for lateral flow generated when the particles leave the downwash region. Smaller cone aperture angles could be helpful to reduce this drift by allowing the droplets to be contained in the high-velocity wake region until they are very close to the ground. It is worth mentioning that small particles (<100 µm) represent a small volume fraction of the sprayed liquid due to the cubic relationship between diameter and volume. Another elucidative result is how when rotors are off, the particle distribution becomes stratified by diameters.

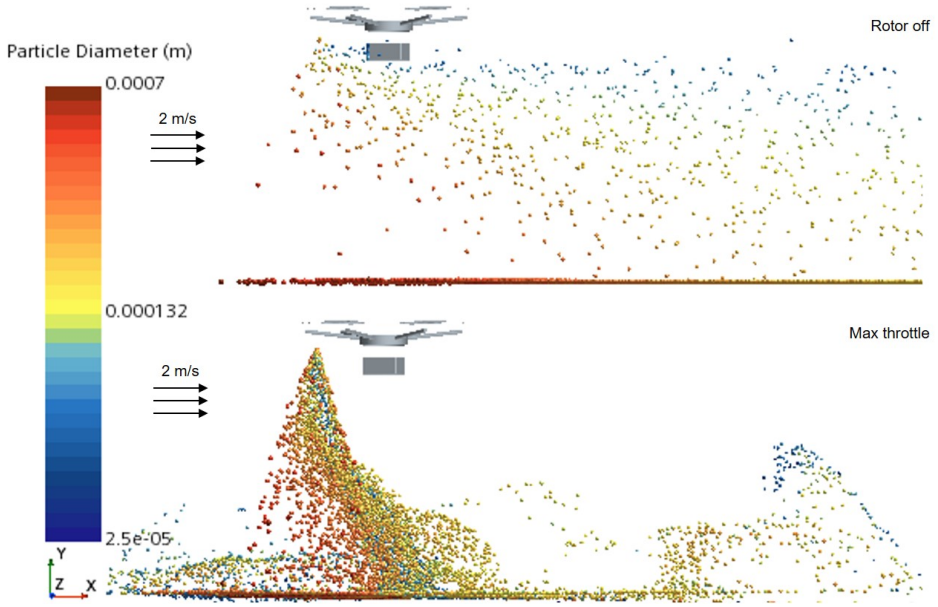

Figure 24. Comparison between droplet distribution in CFD simulations at a wind speed of 2 $m \cdot s^{-1}$ with rotors off (**top**) and rotors at full throttle (**bottom**).

5. Discussion

The enhanced performance obtained with the rotor-on configuration was expected, as the particles with small inertia align with the streamlines of the flow, which, in this case, are directed towards the ground. In the case of rotors-off, these are horizontal, and droplets drift for long distances. In an actual flight, this situation would be equivalent to positioning the injectors to avoid the hexacopter's wake. In this case, particles are not convected downstream of the UASS but remain suspended in the air for a long time and could be transported very long distances, even by small wind gusts. This situation should be avoided from a health point of view, as plant protection products (PPP) are often hazardous, but also from an efficiency point of view, as a reasonable amount of the product would miss the plant. Another conclusion that can be drawn from this study is that when the rotor's wake is used to enhance spray prediction, conventional nozzles will probably perform better compared to anti-drift nozzles. This suggestion is derived from the fact that particles with the large inertia typically generated by anti-drift nozzles will escape the positive wake influence. On the other hand, in a non-wake-influence situation, the opposite scenario would be found, as particles with large inertia would maintain the cone structure, and smaller particles would drift away for long distances. Both situations shown in Figure 24 are identical, with the only difference being the blade rotation rate. This fact also emphasizes the vital role of this operation parameter in droplet deposition, which is especially important to study as the weight of UASSs may vary significantly during their mission, with ratios of up to 40% comparing final and initial weight. An additional comment that arises from this activity is the need to avoid the formation of so-called horseshoe vortices, also known as super-tip vortices in the field of urban air mobility [41], typically formed in multicopter wakes operating at relatively high advance velocities [4,24]. Otherwise, the spray footprint would become much more unpredictable and difficult to control, even though it could have some benefits, such as better lateral penetration of the plant.

Another aspect studied during this work is the definition of an optimal nozzle position below the rotors. The authors are unaware of any previous work regarding optimal nozzle positioning. The first consideration is that every advance velocity and rotation rate combination would require a different position due to bending of the rotors' wake. The variation of the blade rotation rate caused by the decrease in the payload requires different nozzle positions, and therefore a compromise solution should be adopted. Figure 25 shows

the averaged velocity magnitude in the region below the arms of the multicopter where the injectors will be placed. Even though this is a highly complex non-linear optimization problem, it seems reasonable to place the injector in a position where most of the particles' paths will encounter the higher velocity regions as much as possible. According to this reasoning, a good position would be to place the nozzle in the central region. This location will allow that when the cone opens, all particle trajectories will be the maximum distance under the influence of high velocities before leaving the stream tube. This preliminary hypothesis is supported by the experimental results varying the radial and vertical position of the nozzle presented in [26]. However, an extensive dedicated numerical campaign is needed to verify our initial findings, in which several nozzle positions and orientations should be studied for different forward speeds.

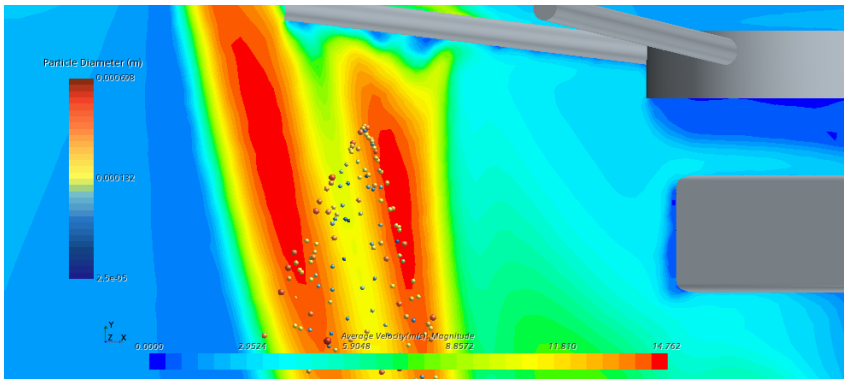

Figure 25. Velocity magnitude averaged during 10 rotor revolutions in CFD simulations with a wind speed of 2 $m \cdot s^{-1}$ and rotors operating at 5100RPM.

6. Conclusions and Future Works

The experimental procedure is based on lateral and frontal photographs of the flow, with a large field of view necessary to validate the spray pattern obtained in the CFD simulations. This prevents us from obtaining sufficient spatial resolution to compute individual droplet statistics. The adopted methodology allows the determination of spray contours, which allows both qualitative validation of the CFD model and evaluation of the effect of different operation parameters on spray drift.

The effect that flight speed and rotation rate have on spray distributions in the wake of a hexacopter is highlighted in the present study. Spray distributions under different operating conditions have been explored numerically using CFD simulations and experimentally in a series of wind tunnel tests. Numerical predictions agree with experimental data in two cases showing very different spray contours, providing confidence in the implemented approach.

In particular, this work is focused on the beneficial effect that positioning the nozzles in the wake of the rotors has in mitigating drift. The improvement in precision operations has been demonstrated by comparing spray distributions at a flight speed of 2 $m \cdot s^{-1}$ with and without rotors on. Similarly, experimental results show that for a given velocity, increasing the rotation rate reduces the spray drift. This finding is significant, considering the weight of a UASS can decrease up to around 40% due to spraying. Similarly, increasing the flight velocity increases spray drift for a given rotation rate. These results suggest that the non-dimensional ratio between flight and blade tip velocity will become a critical design parameter for efficient precision spray operations.

Frontal images obtained in the experimental campaign reveal that when nozzles are placed below operating rotors, the spray cone angle closes. This result has been corroborated by CFD simulations using the volume-of-fluid approach, which reveals a reduction from 80 to 56 degrees. This reduction becomes relevant in precision operations as lateral areas may not be reached due to the cone closure. To overcome this limitation, the flight altitude and the nozzle must be adjusted.

Lagrangian multiphase CFD simulations provide relevant information for nozzle selection and positioning. A very significant influence of the nozzle diameter on the drift is detected. Smaller particles become much more susceptible to drift and are more affected by the rotor wake due to their reduced inertia. Two additional preliminary considerations can be drawn from this study regarding nozzle positioning. The first conclusion is that the optimal nozzle position depends on flight speed and rotation rate. The second is that the location of the nozzles should aim to ensure the droplet trajectories are immersed in high vertical velocity regions for the longest possible distance to allow sufficient injection of momentum towards the target.

Future work will include an extensive numerical campaign using the validated numerical model to obtain more insight into optimal nozzle positioning and the detailed effect of other operational parameters. In this regard, we are carrying out an in-depth study and experimental testing of nozzles, beginning with the model HCI8002, through particle/droplet image analysis (PDIA) methods to improve the accuracy of the numerical model. Furthermore, we will compare the results of the simulations with data obtained in a flight test campaign both in the wind tunnel and the vineyard.

Author Contributions: Conceptualization, M.C.R., N.B., G.G. and D.D.; methodology, M.C.R., N.B., G.G. and D.D.; software, M.C.R., N.B. and D.D.; validation, M.C.R. and N.B.; formal analysis, M.C.R. and N.B.; investigation, M.C.R., N.B., G.G. and D.D.; resources, M.C.R., N.B., G.G. and D.D.; data curation, M.C.R. and N.B.; writing—original draft preparation, M.C.R. and N.B.; writing—review and editing, G.G. and D.D.; visualization, M.C.R. and N.B.; supervision, G.G. and D.D.; project administration, G.G.; funding acquisition, G.G. All authors have read and agreed to the published version of the manuscript.

Funding: This research activity relies on funds from the project "New technical and operative solutions for the use of drones in Agriculture 4.0" (Italian Ministry of University and Research—Progetti di Ricerca di Rilevante Interesse Nazionale—PRIN 2017, Prot. 2017S559BB).

Data Availability Statement: Not applicable.

Acknowledgments: The authors gratefully acknowledge the support and would like to thank MAVTech S.r.l. for the design and realization of structural and mechanical parts, ARAG Group for the particle diameter distribution of the nozzle studied, and the SEASTAR Competence Center for allowing the free use of the SEASTAR Wind Tunnel, and in particular, Raffaella Gerboni for her patient support. The authors would also like to acknowledge the support of and would like to thank the Quality and Metrology Laboratories of the Department of Management and Production Engineering (DIGEP) at Politecnico di Torino for the optical scanning of the rotor blade geometry.

Conflicts of Interest: The authors declare no conflict of interest.

Abbreviations

The following abbreviations are used in this manuscript:

UAS	unmanned aerial system
UASS	unmanned aerial spraying system
CFD	computational fluid dynamics
PA	precision agriculture
DPM	dispersed phase model
LED	light-emitting diode
VOF	volume of fluid
SEASTAR-WT	Sustainable Energy Applied Sciences, Technology, and Advanced Research Wind Tunnel
OPMM	optical precision measuring machine
MTOW	maximum take-off weight
RGB	red, green, blue
URANS	unsteady Reynolds-averaged Navier–Stokes

AMI	arbitrary mesh interface
AMR	adaptive mesh refinement
CSF	continuum surface force
CFL	Courant–Friedrich–Levy
CAD	computer-aided design
PPP	plant protection product

References

1. Saleem, M.H.; Potgieter, J.; Arif, K.M. Automation in agriculture by machine and deep learning techniques: A review of recent developments. *Precis. Agric.* **2021**, *22*, 2053–2091. [CrossRef]
2. Idoje, G.; Dagiuklas, T.; Iqbal, M. Survey for smart farming technologies: Challenges and issues. *Comput. Electr. Eng.* **2021**, *92*, 107104. [CrossRef]
3. Radoglou-Grammatikis, P.; Sarigiannidis, P.; Lagkas, T.; Moscholios, I. A compilation of UAV applications for precision agriculture. *Comput. Netw.* **2020**, *172*, 107148. [CrossRef]
4. Bloise, N.; Carreño Ruiz, M.; D'Ambrosio, D.; Guglieri, G. Preliminary design of a remotely piloted aircraft system for crop-spraying on vineyards. In Proceedings of the 2020 IEEE International Workshop on Metrology for Agriculture and Forestry (MetroAgriFor), Trento, Italy, 4–6 November 2020; IEEE: Piscataway, NJ, USA, 2020; pp. 1–6.
5. He, X. Rapid development of unmanned aerial vehicles (UAV) for plant protection and application technology in China. *Outlooks Pest Manag.* **2018**, *29*, 162–167. [CrossRef]
6. Nuyttens, D.; Baetens, K.; De Schampheleire, M.; Sonck, B. Effect of nozzle type, size and pressure on spray droplet characteristics. *Biosyst. Eng.* **2007**, *97*, 333–345. [CrossRef]
7. Chen, S.; Lan, Y.; Zhou, Z.; Ouyang, F.; Wang, G.; Huang, X.; Deng, X.; Cheng, S. Effect of droplet size parameters on droplet deposition and drift of aerial spraying by using plant protection UAV. *Agronomy* **2020**, *10*, 195. [CrossRef]
8. Ahmad, F.; Qiu, B.; Dong, X.; Ma, J.; Huang, X.; Ahmed, S.; Chandio, F.A. Effect of operational parameters of UAV sprayer on spray deposition pattern in target and off-target zones during outer field weed control application. *Comput. Electron. Agric.* **2020**, *172*, 105350. [CrossRef]
9. Wang, G.; Han, Y.; Li, X.; Andaloro, J.; Chen, P.; Hoffmann, W.C.; Han, X.; Chen, S.; Lan, Y. Field evaluation of spray drift and environmental impact using an agricultural unmanned aerial vehicle (UAV) sprayer. *Sci. Total Environ.* **2020**, *737*, 139793. [CrossRef]
10. Faiçal, B.S.; Freitas, H.; Gomes, P.H.; Mano, L.Y.; Pessin, G.; de Carvalho, A.C.; Krishnamachari, B.; Ueyama, J. An adaptive approach for UAV-based pesticide spraying in dynamic environments. *Comput. Electron. Agric.* **2017**, *138*, 210–223. [CrossRef]
11. Scagnellato, L.; Lecce, M.; Bloise, N.; Carreño Ruiz, M.; Capello, E.; Guglieri, G. Adaptive path planning for spraying UAS in vineyard under variable wind condition. In Proceedings of the ICAS 2022, Stockholm, Sweden, 4–9 September 2022.
12. Meng, Y.; Su, J.; Song, J.; Chen, W.H.; Lan, Y. Experimental evaluation of UAV spraying for peach trees of different shapes: Effects of operational parameters on droplet distribution. *Comput. Electron. Agric.* **2020**, *170*, 105282. [CrossRef]
13. Martinez-Guanter, J.; Agüera, P.; Agüera, J.; Pérez-Ruiz, M. Spray and economics assessment of a UAV-based ultra-low-volume application in olive and citrus orchards. *Precis. Agric.* **2020**, *21*, 226–243. [CrossRef]
14. Wang, C.; Herbst, A.; Zeng, A.; Wongsuk, S.; Qiao, B.; Qi, P.; Bonds, J.; Overbeck, V.; Yang, Y.; Gao, W.; et al. Assessment of spray deposition, drift and mass balance from unmanned aerial vehicle sprayer using an artificial vineyard. *Sci. Total Environ.* **2021**, *777*, 146181. [CrossRef]
15. Li, X.; Giles, D.K.; Niederholzer, F.J.; Andaloro, J.T.; Lang, E.B.; Watson, L.J. Evaluation of an unmanned aerial vehicle as a new method of pesticide application for almond crop protection. *Pest Manag. Sci.* **2021**, *77*, 527–537. [CrossRef]
16. Sarri, D.; Martelloni, L.; Rimediotti, M.; Lisci, R.; Lombardo, S.; Vieri, M. Testing a multi-rotor unmanned aerial vehicle for spray application in high slope terraced vineyard. *J. Agric. Eng.* **2019**, *50*, 38–47. [CrossRef]
17. Biglia, A.; Grella, M.; Bloise, N.; Comba, L.; Mozzanini, E.; Sopegno, A.; Pittarello, M.; Dicembrini, E.; Alcatrão, L.E.; Guglieri, G.; et al. UAV-spray application in vineyards: Flight modes and spray system adjustment effects on canopy deposit, coverage, and off-target losses. *Sci. Total Environ.* **2022**, *845*, 157292. [CrossRef]
18. Zhan, Y.; Chen, P.; Xu, W.; Chen, S.; Han, Y.; Lan, Y.; Wang, G. Influence of the downwash airflow distribution characteristics of a plant protection UAV on spray deposit distribution. *Biosyst. Eng.* **2022**, *216*, 32–45. [CrossRef]
19. Liu, Q.; Chen, S.; Wang, G.; Lan, Y. Drift Evaluation of a Quadrotor Unmanned Aerial Vehicle (UAV) Sprayer: Effect of Liquid Pressure and Wind Speed on Drift Potential Based on Wind Tunnel Test. *Appl. Sci.* **2021**, *11*, 7258. [CrossRef]
20. Grant, S.; Perine, J.; Abi-Akar, F.; Lane, T.; Kent, B.; Mohler, C.; Scott, C.; Ritter, A. A Wind-Tunnel Assessment of Parameters That May Impact Spray Drift during UAV Pesticide Application. *Drones* **2022**, *6*, 204. [CrossRef]
21. Chen, P.; Douzals, J.P.; Lan, Y.; Cotteux, E.; Delpuech, X.; Pouxviel, G.; Zhan, Y. Characteristics of unmanned aerial spraying systems and related spray drift: A review. *Front. Plant Sci.* **2022**, 2726. [CrossRef]
22. Zhang, H.; Qi, L.; Wu, Y.; Musiu, E.M.; Cheng, Z.; Wang, P. Numerical simulation of airflow field from a six–rotor plant protection drone using lattice Boltzmann method. *Biosyst. Eng.* **2020**, *197*, 336–351. [CrossRef]
23. Yang, F.; Xue, X.; Cai, C.; Sun, Z.; Zhou, Q. Numerical simulation and analysis on spray drift movement of multirotor plant protection unmanned aerial vehicle. *Energies* **2018**, *11*, 2399. [CrossRef]

24. Wen, S.; Han, J.; Ning, Z.; Lan, Y.; Yin, X.; Zhang, J.; Ge, Y. Numerical analysis and validation of spray distributions disturbed by quad-rotor drone wake at different flight speeds. *Comput. Electron. Agric.* **2019**, *166*, 105036. [CrossRef]
25. Wang, L.; Xu, M.; Hou, Q.; Wang, Z.; Lan, Y.; Wang, S. Numerical verification on influence of multi-feature parameters to the downwash airflow field and operation effect of a six-rotor agricultural UAV in flight. *Comput. Electron. Agric.* **2021**, *190*, 106425. [CrossRef]
26. Bloise, N.; Carreño Ruiz, M.; D'Ambrosio, D.; Guglieri, G. Wind Tunnel Testing of Remotely Piloted Aircraft Systems for Precision Crop-Spraying Applications. In Proceedings of the 2021 IEEE International Workshop on Metrology for Agriculture and Forestry (MetroAgriFor), Trento-Bolzano, Italy, 3–5 November 2021; IEEE: Piscataway, NJ, USA, 2021; pp. 378–383.
27. Bloise, N.; Carreño Ruiz, M.; Mai, E.; D'Ambrosio, D.; Guglieri, G. Analysis and Design of Unmanned Aerial Systems for Precision Agriculture applications on Vineyards. In Proceedings of the EUCASS 2022, Lille, France, 3–8 July 2022.
28. Di Martino, M.; Ahirwal, D.; Maffettone, P.L. Three-dimensional computational fluid dynamics simulation of the hollow-cone spray process: The stability of the conical liquid sheet. *Phys. Fluids* **2021**, *33*, 063301. [CrossRef]
29. Laurila, E.; Roenby, J.; Maakala, V.; Peltonen, P.; Kahila, H.; Vuorinen, V. Analysis of viscous fluid flow in a pressure-swirl atomizer using large-eddy simulation. *Int. J. Multiph. Flow* **2019**, *113*, 371–388. [CrossRef]
30. Gerboni, R.; Ledda, G.; Moscatello, A.; Uggenti, A.C.; Carpignano, A. Fluid-Dynamic Calibration of an Atmospheric Wind Tunnel Applied to Test Offshore Infrastructures. In Proceedings of the OMC Med Energy Conference and Exhibition, Ravenna, Italy, 28–30 September2021; OnePetro: Richardson, TX, USA, 2021.
31. Siemens PLM Software Inc. *STAR-CCM+ User Guide Version 14.06*; Siemens PLM Software Inc.: Plano, TX, USA, 2019.
32. Carreño Ruiz, M.; Scanavino, M.; D'Ambrosio, D.; Guglieri, G.; Vilardi, A. Experimental and numerical analysis of multicopter rotor aerodynamics. In Proceedings of the AIAA Aviation 2021 Forum, Virtual Event, 2–6 August 2021; p. 2539.
33. Carreño Ruiz, M.; Manavella, A.; D'Ambrosio, D. Numerical and experimental validation and comparison of reduced order models for small scale rotor hovering performance prediction. In Proceedings of the AIAA SCITECH 2022 Forum, San Diego, CA, USA, 24–26 October 2022; p. 0154.
34. Carreño Ruiz, M.; Scanavino, M.; D'Ambrosio, D.; Guglieri, G.; Vilardi, A. Experimental and numerical analysis of hovering multicopter performance in low-Reynolds number conditions. *Aerosp. Sci. Technol.* **2022**, *128*, 107777. [CrossRef]
35. Spalart, P.; Allmaras, S. A one-equation turbulence model for aerodynamic flows. In Proceedings of the 30th Aerospace Sciences Meeting and Exhibit, Reno, NV, USA, 6–9 January 1992.
36. Schiller, L. Über die grundlegenden Berechnungen bei der Schwerkraftaufbereitung. *Z. Vereines Dtsch. Inge.* **1933**, *77*, 318–321.
37. Sommerfeld, M. Theoretical and experimental modelling of particulate flows. *VKI Lect. Ser.* **2000**, *6*, 3–7.
38. Brackbill, J.U.; Kothe, D.B.; Zemach, C. A continuum method for modeling surface tension. *J. Comput. Phys.* **1992**, *100*, 335–354. [CrossRef]
39. Lefebvre, A.H.; McDonell, V.G. *Atomization and Sprays*; CRC Press Boca Raton, FL, USA, 2017.
40. Akima, H. A new method of interpolation and smooth curve fitting based on local procedures. *J. ACM (JACM)* **1970**, *17*, 589–602. [CrossRef]
41. Ventura Diaz, P.; Yoon, S. High-Fidelity Simulations of a Quadrotor Vehicle for Urban Air Mobility. In Proceedings of the AIAA SCITECH 2022 Forum, San Diego, CA, USA, 3–7 January 2022; p. 0152.